Design and numerical simulation of a DNA electrophoretic stretching device†

Ju Min Kim and Patrick S. Doyle*

Received 22nd August 2006, Accepted 14th November 2006
First published as an Advance Article on the web 15th December 2006
DOI: 10.1039/b612021k

DNA stretching is now a key technology in emerging DNA mapping devices such as direct linear analysis (DLA), though DNA stretching in a high throughput manner is still a challenging problem. In this work, we present a new microfluidic channel design to enhance DNA stretching using kinematic analysis and Brownian dynamics-finite element method (BD-FEM). Our group recently showed in experiments that the extensional electrophoretic field arising from a hyperbolic microcontraction can be utilized to stretch T4-DNA. We demonstrate the reliability of our BD-FEM model for the present problem by showing that the numerical predictions are consistent with the experimental data for the hyperbolic channel. We then investigate DNA stretching for four different funnel shapes. Surprisingly the maximum mean DNA stretch is quite similar in all four designs. Finally, we propose a new design with a side-feeding branch to enhance stretching based on a kinematic analysis along different feeding locations. Our numerical simulation predicted that DNA stretching can be dramatically enhanced using side-feeding.

Introduction

The information extracted from DNA has long been used as a basis for molecular biological studies such as genomics and proteomics. The traditional method based on polymerase chain reaction (PCR)/gel-electrophoresis has been extensively utilized for DNA sequencing with single base-pair resolution.[1] On the other hand, lower-resolution genomic mapping techniques[2] have recently attracted much attention in comparative genomic studies due to their low cost, efficiency and speed. In many cases, the non-gel-based lower resolution method is sufficient to identify a species and discern differences such as mutations in the same species.[2,3] The lower-resolution technique can also be utilized as a complementary method to improve the accuracy of the whole genome sequencing, specifically in analyzing large DNA.[4]

The lower-resolution methods are typically based on fluorescent microscopy combined with DNA stretching technology. One successful example is a restriction enzyme method combined with optical measurement. Schwartz *et al.*[5] developed a restriction mapping method, and Dimalanta *et al.*[6] developed a way to stretch DNA using capillary force-driven flow in microfluidic channels that contain aminosilane-treated surfaces for DNA fixation. It has been also shown that nanochannels can be used to stretch DNA for restriction mapping.[7,8]

Another promising lower-resolution method is direct linear analysis (DLA), which involves stretching DNA in microcontraction flows.[2,3,9–11] In DLA, DNA molecules with fluorescent probes attached to specific sequences are stretched with field gradients within microchannels and the distances between adjacent probes are measured by optical methods.[2,3] The unique length between probes in the DLA method will be preserved only in a fully stretched state. Thus, DNA dynamics in non-homogeneous field gradients are a major focus due to their practical importance in such lower-resolution DNA mapping techniques, in addition to fundamental polymer physics.[2,3,9–13]

Randall and Doyle showed that DNA hooking around a cylindrical obstacle of which the radius is comparable to the DNA size (radius of gyration) is strongly dependent upon field gradients, *i.e.*, local strain rate and principal axes of stretching and compression.[14] Randall and Doyle also found that DNA experience stretching-compression-stretching according to local field kinematics around a rather large obstacle as DNA travels past the obstacle.[12] Thus, it could be concluded that local field kinematics plays an essential role in DNA deformation. They also observed that 'molecular individualism',[15] which denotes the strong dependency of DNA dynamics on the initial configuration, is still relevant in non-homogeneous fields and stretching-compression-stretching dynamics are observed in DNA electrophoresis past a cylinder.

Later, Kim and Doyle developed a numerical simulation technique to simulate DNA electrophoresis in non-homogeneous electric fields using BD-FEM.[13] They showed that the predicted results are qualitatively and quantitatively consistent with the previous experiments of Randall and Doyle,[12] *e.g.* 'molecular individualism' is obtained in non-homogeneous fields.

Based on the first principles found in the studies of DNA deformation around obstacles, Randall *et al.*[10] developed and analyzed a DNA stretching device using electrophoresis in hyperbolic microcontraction geometries. They showed that the probability density of fractional stretching is rather broad at the exit of the hyperbolic channel and attributed this to

Department of Chemical Engineering, Massachusetts Institute of Technology, Cambridge, MA 02139, USA. E-mail: pdoyle@mit.edu; Fax: (617) 258-5042; Tel: (617) 253-4534

† Electronic supplementary information (ESI) available: The molecules shown in Fig. 1(b) and (c) with channel boundary to show the position of DNA; non-dimensionalized strain rate and strain for case II of Table 1. See DOI: 10.1039/b612021k

'molecular individualism' and the finite strain experienced by molecules. According to a previous study on polymer stretching in planar extensional flow,[16] the stretching attains a steady-state distribution after strain ~ 10. However, the computed strain along the centerline of the device in ref. 10 is limited to ~ 4. Inspired by the previous study of the pre-shearing effect on DNA stretching,[17] Randall *et al.*[10] proposed a way to overcome 'molecular individualism' using 'preconditioning' by introducing a gel-region just before the contraction region. They observed that DNA is partially stretched at the exit of the gel-region due to a quasi-tethering effect and the fractional stretching of DNA is dramatically increased with quite narrow probability distribution even for moderate strains.

The main objectives of the present study are to directly compare the numerical predictions of our BD-FEM method with the available experimental data for DNA stretching in microcontractions and to explore the possibility of enhancing DNA stretching with new channel designs. First, we perform a kinematic analysis of the electric field and then, we use the BD-FEM method to consider new design choices: funnel shapes and DNA feeding location. We link the results with the kinematic analysis. We expect that our new designs will be useful for the practical implementation of DNA stretching devices using electrophoresis.

Background theory

We briefly describe the theoretical background for DNA deformation in electric fields in *confined geometries*. The Debye length (κ^{-1}) around the DNA phosphate backbone is typically O (nm) in concentrated salt solutions, which is much smaller than DNA's persistence length (A_p) and contour length (L). We consider a TOTO-1 stained double strand T4-DNA (4.7 : 1, bp : dye)[10] with 169 kbp as a model system. Its contour length is approximately 71.4 μm which is estimated from extrapolating results for 48.5 kbp λ-DNA (stained contour $\approx$ 20.5 μm).[13] Since there is still uncertainty about the persistence length A_p for stained DNA, we use A_p corresponding to the unstained DNA persistence length[18] (0.053 μm). Thus, since $\kappa^{-1} \ll A_p \ll L$, we can ignore local electric field disturbances by DNA movement and thus, DNA behaves like a neutral polymer free from the effects of electrostatic potential among DNA segments.[19]

The electric field ($\boldsymbol{E}$) can be obtained with the relationship $\boldsymbol{E} = -\nabla\Phi$ from the potential equation ($\nabla^2\Phi = 0$) for given boundary conditions, where Φ is an electric potential. In electric fields, a non-Brownian charged-particle moves according to the electrophoretic velocity field ($\mu\boldsymbol{E}$), where μ is the electrophoretic mobility, and we preclude non-linear electrophoretic effects, though they might be important in high electric fields as discussed by Randall *et al.*[10] Our group has shown that the kinematics for an electrophoretic field are purely extensional, *i.e.* shear-free, and DNA deforms around an obstacle according to local kinematics such as electrophoretic strain rate ($\dot{\epsilon}^{EL}$) and principal axes of stretching and compression.[12,13] We discussed that considering local kinematics is essential in accurately predicting DNA stretching in non-homogenous electric fields.[13]

The flow disturbance by a charged-bead quickly decays due to the compensating movement of counterions in the case of small Debye lengths.[19] Consequently, DNA shows a freely-draining behavior in uniform electric fields, and its mobility is size-independent since driving forces and drag forces scale linearly with molecular weight. Long *et al.*[19] showed that DNA dynamics can be analyzed with the classical Zimm paradigm[20] irrespective of the sources of background fields (hydrodynamic-driven velocity $\boldsymbol{u}^{\infty}$ or electrophoretic $\mu\boldsymbol{E}$ fields), *i.e.*, the flow disturbance by DNA movement due to electric field is restricted to $<\kappa^{-1}$, and hydrodynamic disturbances by other forces such as spring and Brownian forces can be modeled with an Oseen tensor, which is now known as 'electro-hydrodynamic equivalence'.[19,21]

In bulk flows, hydrodynamic interaction (HI) plays an important role due to its long range property ($\sim 1/r$), which results in collective behaviors. However, in a confined geometry, HI decays relatively quickly ($\sim 1/r^2$).[22] Tlusty[23] and Balducci *et al.*[24] showed that HI can be screened in thin slits. Since the radius of gyration (R_g) of T4-DNA (1.4 μm) is comparable with the gap height h (2 μm) and $L \gg h$, in the present work, we assume that HI is screened, and thus, we adopt a freely-draining model. In experiments, HI screening has also been observed in confined geometries.[24–26]

The principal non-dimensional group is the Deborah number as $De = \tau \times \dot{\epsilon}^{EL}$ for the DNA stretching problem, where τ is the longest relaxation time of a molecule. We define accumulated strain ϵ following a trajectory as $\epsilon = \int_{path} \dot{\epsilon}^{EL} \Big/ \left|\mu\boldsymbol{E}(s)\right| ds$. One limiting condition of DNA stretching is affine deformation according to field kinematics. The extent of affine deformation is $\Delta = \Delta_0 \exp(\epsilon)$, where Δ_0 is the initial infinitesimal distance between two points in a field and Δ is the distance after the strain ϵ. However, in reality, DNA deformation deviates from an ideal affine deformation due to a non-linear spring force and Brownian motion, *i.e.*, other forces such as spring and Brownian forces are competing with electric forces. This competition is also responsible for the famous 'coil-stretch transition'.[27] DNA preserves a coiled state due to internal spring forces at low De, and DNA starts to strongly stretch over a critical De (refer to a review by Shaqfeh[28]). This criterion is kinematic history-dependent in non-homogeneous fields.[29] The rate of DNA stretching is also highly dependent upon the initial configuration, a form of 'molecular individualism',[15] and thus, DNA apparently shows chaotic stretching in field gradients.

Finally, we comment that 'excluded volume interactions' are included in modeling DNA since experiments are performed using good solvents. We also assume that electro-osmotic flow is eliminated by polymer-coating on the channel walls as it was done in experiments.[10,12,30]

Microcontraction geometry and kinematics

Geometry

We present a schematic diagram for simulating DNA stretching in a hyperbolic channel in Fig. 1(a), which was designed to mimic the previous experimental apparatus.[10] w_1 and l_1 denote half of the upstream width and the full upstream length, respectively, and w_2 and l_2 correspond to half of the downstream width and the full downstream length, respectively. The shape of the contraction region is

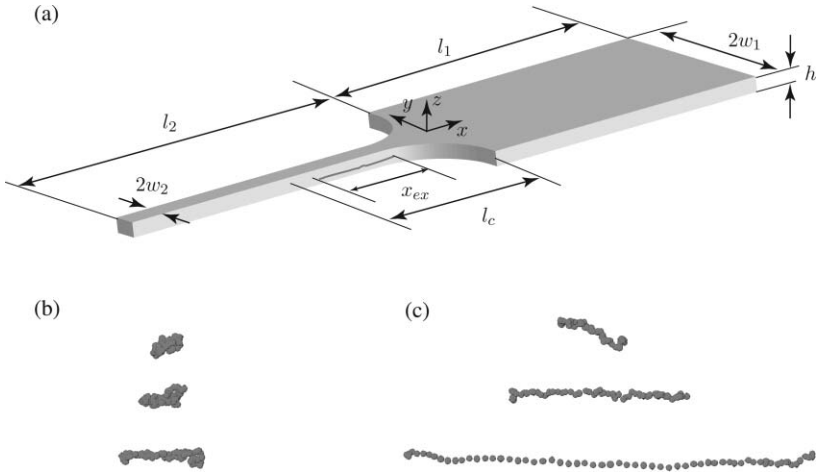

Fig. 1 (a) A schematic diagram for a hyperbolic channel to stretch DNA in electric fields. A stretched DNA (with extension x_{ex}) is shown. (b), (c) A representative result to show 'molecular individualism' at De = 7 in the stretching device (case IV in Table 1). Two molecules, (b) and (c), which move commonly along the centerline, are sampled and thus the molecules experience a similar kinematic history (see ESI† to refer to the relative position of DNA in the device). Times between two successive snapshots in (b) are 0.49, 0.21 and times between snapshots in (c) are 0.77 and 0.15 , respectively.

hyperbolic,[10] $y = C/(x + C/w_1)$, where x is the distance downstream from the starting point of the contraction region, its length is l_c and $C = w_2 l_c/(1 - w_2/w_1)$.[10] The exit of the hyperbolic region is connected to a channel of constant width (w_2). In this work, w_1 and w_2 are 100 μm and 1.9 μm, respectively, and l_c is 80 μm, which are consistent with previous experimental conditions.[10] Both l_1 and l_2 are set to 250 μm to mimic sufficiently long upstream and downstream channels, and it was checked that uniform electric fields are developed in the inlet and outlet regions. The height of the channel (h) is constant and set to 2 μm (to match experimental conditions). The extent of DNA stretching (x_{ex}) is measured as the distance between the downstream-most coordinates (x_d,y_d) and the upstream-most coordinates (x_u,y_u) of a molecule.

Kinematics

In the previous experiments, the hyperbolic geometry in Fig. 1(a) was originally designed to generate a uniform planar extensional field in the hyperbolic region. We computed the electric field using the finite element method which will be described in the next section. For channels of constant thickness, the electric fields are thickness-independent due to the insulating boundary condition ($\frac{\partial \Phi}{\partial n} = 0$) on the PDMS walls, where $\boldsymbol{n}$ is the vector normal to the walls.

We show the electric field components in Fig. 2(a) and (b), where the field is non-dimensionalized with the inlet electric field, E_0. As shown in Fig. 2(a), the acceleration is clear in the hyperbolic region due to the decreasing width of the channel, and there is a rather strong inward field at the side walls in the entrance region as shown in Fig. 2(b). Based on the electrophoretic velocity fields ($\mu \boldsymbol{E}$) where μ is the DNA electrophoretic mobility, we obtained the electrophoretic strain rate ($\dot{\epsilon}^{EL}$) and the principal axes of stretching and compression by solving the eigenvalue/eigenvector problem for the electrophoretic velocity gradient tensor $\nabla \mu \boldsymbol{E}$. The strain rate corresponds to the positive eigenvalue, and its companion eigenvector is the principal axis of stretching. The eigenvector corresponding to negative eigenvalue denotes the principal axis of compression.

We show the non-dimensionalized electrophoretic strain rate distribution in the channel in Fig. 2(c), where the electrophoretic strain rate is non-dimensionalized as $\hat{\epsilon}^{EL} = \dot{\epsilon}^{EL} / (\mu E_0 / l_c)$. We show the quantitative distribution along different initial y-coordinates in Fig. 2(e) and (f). As shown in Fig. 2(c) and (e), $\hat{\epsilon}^{EL}$ is uniform for -80 μm $< x <$ -30 μm ($-1 < x/l_c < -0.38$). However, there are non-negligible entrance effects for -30 μm $< x < 0$ μm ($-0.38 < x/l_c < 0$), and there are overshoot regions along the side-walls. We mention that there is a spike near the wall in the funnel exit region ($x = -80$ μm) as shown in Fig. 2(c) and (e), which is due to the discontinuity between the funnel and the constant width downstream channel. However, since the spike is localized and the residence time is small in this area, there is no significant increase in strain as shown in Fig. 2(f). Thus, we believe that it does not affect DNA stretching.

In Fig. 2(d), we show the sampled principal axes of stretching and compression along three electrophoretic field lines. The black and green lines of each cross correspond to stretching and compression axes, respectively, and the length of lines denotes the relative magnitude of strain rate. The distance between two successive crosses increases in the entrance region along a field line, which shows the acceleration of electrophoretic velocity. When a deformable non-Brownian object moves along a field line, the object will appreciably stretch if the principle axis of stretching is closely aligned with the field direction. Along the centerline, the principal axis of stretching is coincident with the field direction. However, as shown in Fig. 2(d), the direction of the principal axis of stretching rotates away from the x-direction with increasing initial y-coordinate and also does not exactly coincide with the field direction. Thus, the entrance region is kinematically rather complicated. We will study how this entrance region affects the DNA stretching which will be also important for a practical design of a microfluidic channel.

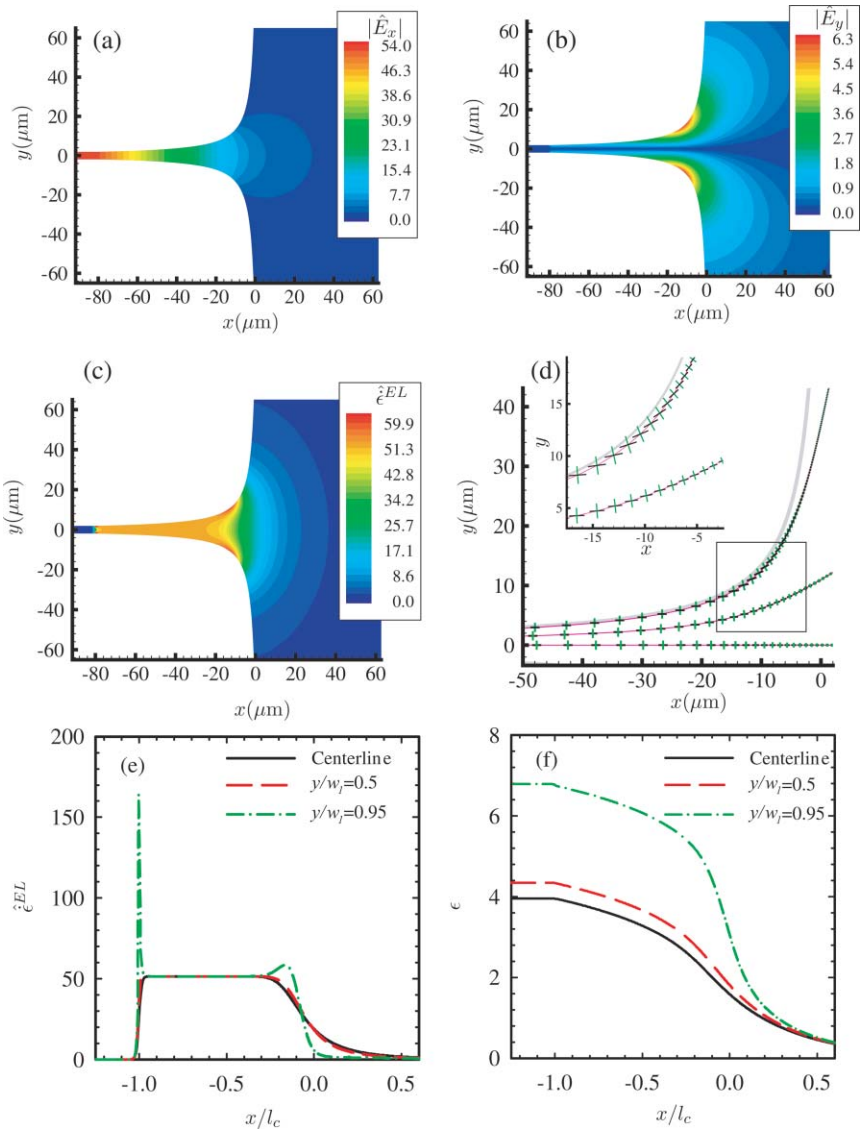

Fig. 2 The kinematic analysis for the hyperbolic channel (case IV in Table 1). Dimensionless electric field: (a) x- and (b) y-components. (c) Non-dimensionalized electrophoretic strain rate distribution in the channel. (d) Each cross denotes the sampled principal axes of stretching and compression along three electrophoretic field lines. The black and green lines of each cross correspond to stretching and compression axes, respectively and the length of lines denotes the relative magnitude of strain rate. The inset in (d) shows a magnified view of the rectangular region. Each field line starts from (x/l_c, y/w_1)=(2.1,0), (2.1,0.5) and (2.1,0.95) successively from the bottom. The thick gray line is the channel boundary. Non-dimensionalized strain rate (e), and strain (f) according to different feeding locations for a hyperbolic channel (case IV in Table 1). These initial conditions correspond to the field lines plotted in Fig. 2(d) and l_c corresponds to the length of the funnel (80 μm).

Numerical model

We presented a method to simulate DNA electrophoresis in complicated geometries in our previous work.[13] Our numerical method is composed of three parts: BD, FEM and the connection algorithm between FEM and BD. DNA is modeled as a bead-spring chain with excluded volume interactions. FEM is adopted to solve the electric field in complicated geometries, and the electric field acts as a forcing term to drive DNA in the bead-spring model. One technical problem is that addressing electric field is not straightforward in complicated geometries composed of unstructured finite element meshes. To accommodate this problem, we devised an efficient way to address electric fields in unstructured meshes called as the 'target-induced searching algorithm',[13] and we developed a modified Heyes–Melrose[13] hard-sphere algorithm to consider bead–wall interactions which prevents a bead from penetrating through walls. We briefly describe the numerical method used in this work and the complete description is presented in our previous work.[13]

Brownian dynamics

DNA is modeled as N_b beads connected by $N_s = (N_b - 1)$ springs. The evolution equation for bead 'i' is:

$$\frac{d\boldsymbol{r}_i}{dt} = \mu^b \boldsymbol{E}(\boldsymbol{r}_i) + \frac{1}{\zeta}\left[\boldsymbol{F}_i^B(t) + \boldsymbol{F}_i^S(t) + \boldsymbol{F}_i^{EV}(t) + \boldsymbol{F}_i^{EV,wall}(t)\right], \quad (1)$$

where μ^b is the mobility of a bead and ζ is the bead drag coefficient, $\boldsymbol{F}_i^B$ the Brownian force, $\boldsymbol{F}_i^S$ the net spring force on the bead, and $\boldsymbol{F}_i^{EV}$ stands for the force due to excluded volume interaction with other beads. $\boldsymbol{F}_i^{EV,wall}$ denotes bead–wall interactions.

In this work, we non-dimensionalize the parameters as follows:

$$\hat{r} \equiv \frac{r}{l}, \hat{t} \equiv \frac{t}{\zeta l^2/k_B T}, \hat{\boldsymbol{E}} \equiv \frac{\boldsymbol{E}}{E_0}, \lambda \equiv \frac{A_{eff}}{A_p}, v \equiv \frac{l}{A_p}, \tag{2}$$

where r is length scale and l stands for the maximum extensible spring length ($\equiv L/N_s$). t is time, k_B is Boltzmann's constant and T is the absolute temperature. E_0 denotes the electric field at the inlet. A_{eff} is an effective persistence length.[31] We model T4-DNA with 64 beads and, thus, 63 springs such that v = 21.4. In addition to primitive variables, dimensionless forces $\hat{\boldsymbol{f}}(\hat{\boldsymbol{r}})$ (spring forces and excluded volume-driven force) are defined as:

$$\hat{\boldsymbol{f}}(\hat{\boldsymbol{r}}) \equiv \frac{\boldsymbol{f}(\boldsymbol{r})l}{k_B T}. \tag{3}$$

The non-dimensionalized form of eqn (4) is:

$$\frac{d\hat{\boldsymbol{r}}_i}{d\hat{t}} = Pe\,\hat{\boldsymbol{E}}(\hat{\boldsymbol{r}}_i) + \hat{\boldsymbol{F}}_i^B + \hat{\boldsymbol{F}}_i^S + \hat{\boldsymbol{F}}_i^{EV} + \hat{\boldsymbol{F}}_i^{EV,wall}, \tag{4}$$

where Pe denotes the bead Peclet number $\mu^b E_0 l/D$ and D is the bead diffusivity $k_B T/\zeta$. The non-dimensional forces are:

$$\hat{\boldsymbol{F}}_i^B = \sqrt{\frac{24}{\delta\hat{t}}}(\boldsymbol{r}_n)_i, \tag{5}$$

$$\hat{\boldsymbol{F}}_i^S = \begin{cases} \hat{\boldsymbol{f}}_{i,N_b-1}^s & i = N_b; \\ \hat{\boldsymbol{f}}_{i,i+1}^s + \hat{\boldsymbol{f}}_{i,i-1}^s & 1 < i < N_b; \\ \hat{\boldsymbol{f}}_{i,2}^s & i = 1, \end{cases} \tag{6}$$

where the spring force $\hat{\boldsymbol{f}}_{i,j}^s$ is modeled using a modified Marko–Siggia spring force,[31,32]

$$\hat{\boldsymbol{f}}_{i,j}^s = \frac{v}{\lambda}\left\{\hat{r}_{ji} - \frac{1}{4} + \frac{1}{4(1-\hat{r}_{ji})^2}\right\}\frac{\hat{\boldsymbol{r}}_j - \hat{\boldsymbol{r}}_i}{\hat{r}_{ji}}. \tag{7}$$

We obtain λ = 1.3875 using the method proposed by Underhill and Doyle[31] and thus, A_{eff} is $\sim$0.0735 μm. The excluded volume force $\hat{\boldsymbol{F}}_i^{EV}$ is modeled with the soft potential devised by Jendrejack *et al.*[33–35]

$$\hat{\boldsymbol{F}}_i^{EV} = -\sum_{j=1(j\neq i)}^{N_b} \frac{9}{2}\hat{v}^{ev,p}\left(\frac{3}{4\sqrt{\pi}}\right)^3 v^{9/2}\exp\left[-\frac{9}{4}v\hat{r}_{ij}^2\right]\hat{\boldsymbol{r}}_{ji}, \tag{8}$$

where r_{ji} denotes the distance between $\boldsymbol{r}_j$ and $\boldsymbol{r}_i$ and $\hat{v}^{ev,p}$ stands for $v^{ev,p}/l^3$, where $v^{ev,p}$ is the parameter for excluded volume.[33–35] $(\boldsymbol{r}_n)_i$ are uniform random numbers such that each component $(r_n)_1^j \in [-1/2,1/2]$, where coordinate number j = x,y,z.

Bead interactions with boundaries $\hat{\boldsymbol{F}}_i^{EV,wall}$ are treated with a modified Heyes–Melrose algorithm.[13,36] Practically, it is implemented such that a bead is re-positioned to the nearest wall whenever it penetrates through the wall during a time step as follows:

$$\Delta\hat{\boldsymbol{r}}_i^{HM} = \Delta\boldsymbol{p}_i H(\Delta p_i), \tag{9}$$

where $\Delta\hat{\boldsymbol{r}}_i^{HM}$ is the displacement vector by the Heyes and Melrose algorithm[36] and Δp_i denotes the minimum distance from the boundary. $\Delta\boldsymbol{p}_i$ is a vector connecting a bead and the boundary point where the distance between the bead center and the boundary point is a minimum. The Heaviside step function is used to consider only the penetrated beads.[36]

FEM, and connection algorithm between BD and FEM

In this work, we use the Galerkin finite element method as a spatial discretization scheme for the governing equation. The governing equation for electrostatic potential is as follows:

$$\nabla^2\Phi = 0 \quad \text{in } \Omega, \tag{10}$$

$$\Phi = \Phi_{given} \quad \text{or} \quad \frac{\partial\Phi}{\partial\boldsymbol{n}} = 0 \quad \text{on } \partial\Omega, \tag{11}$$

where eqn (11) denotes boundary conditions on boundary $\partial\Omega$. On the inlet and outlet, the essential boundary condition (Φ = Φ_{given}) is imposed, whereas the insulating boundary condition ($\frac{\partial\Phi}{\partial n} = 0$) is imposed on the PDMS walls. The above equation is solved with FEM, and Φ is interpolated with a 6-node P_2^0 shape function. We solve the linear equation resulting from FEM discretization with boundary conditions using an iterative solver. After the electrostatic potential (Φ) is obtained, the electric field is computed by the relationship ($\boldsymbol{E} = -\nabla\Phi$), where $\boldsymbol{E}$ is interpolated with a 3-node P_1^0 shape function. Once the electric field is computed, the electric field per node is saved into a database. Whenever the electric field is necessary at specific coordinates, the 'target-induced searching algorithm' is called (see ref. 13 for details), and the finite element which includes the specific coordinate is found. The coordinate in the element is mapped onto the master element coordinate, and then, the electric field is interpolated with a 3-node P_1^0 shape function for a given master element coordinate.[13]

Parameters

The characteristic electrophoretic strain rate for De is defined as $\mu E_1/l_c$, where μE_1 is the electrophoretic velocity in the downstream portion of the channel. This definition is consistent with the definition in previous experiments.[10] The computed T4-DNA radius of gyration in the unconfined state (using 250 independent trajectories) is 1.42 $\pm$ 0.02 μm when $v^{ev,p}$ = 0.0004 μm^3, which is close to the value 1.44 μm extrapolated from available experimental datum for λ-DNA (0.69 μm).[26] The non-dimensional relaxation time was computed to be 6.51 using an ensemble of 500 trajectories in a 2 μm channel with the same method as the previous work.[13] We computed the electric field using FEM explained in the previous section, and the mesh is selected from mesh refinement test to guarantee the accuracy of electric field. We used an extremely fine mesh composed of 426 036 triangular

meshes. The unknowns for the potential field is 855 531 and the electric field is computed using 214 748 vertices nodes.

In this work, 300 DNA molecules are used for the computation of ensemble-averaged values. Throughout this study, if there is no special comment, the initially equilibrated DNA in the channel is placed at $x_c/l_c = 2.1$ with a uniform random distribution of $y_c/w_1 \in [-1,1]$, where (x_c,y_c) denotes the coordinates for the center of mass of DNA. The initial location is rejected and regenerated in cases where part of the DNA penetrates through side walls. We selected $x/l_c = 2.1$ as an initial condition because here $\hat{\epsilon}^{EL}$ is very small so we can assume that the DNA is initially in an equilibrium configuration.

The time-stepping algorithm that we used is an 'adaptive' time-stepping scheme described in the previous work.[13] The time step $\delta\hat{t}$ is set to 10^{-2} at De = 14 until the x-component of the center of mass of DNA passes 0, and then $\delta\hat{t}$ is re-scaled to 10^{-3}. This scheme is considered to speed up computational time since DNA experiences negligible deformation with slow movement in the upstream region, which results in the consumption of most computational time in this stage. We also checked a smaller time step of $\delta\hat{t} = 10^{-3}$ at De = 14 in the upstream region and then, re-scaled to $\delta\hat{t} = 10^{-4}$ after the x-component of the center of mass of DNA passes 0. There is no appreciable difference between the smaller time step and original time step in the predicted mean ensemble fractional stretching at the exit of the hyperbolic region. The upstream $\delta\hat{t}$ scales as $\sim 1/\mathrm{De}$ for De $>$ 14 and the rescaled $\delta\hat{t}$ is always 0.1 times the upstream $\delta\hat{t}$. The upstream $\delta\hat{t}$ is fixed to 10^{-2} for De lower than 14 due to the convergence problem during the computation of the spring forces.[13]

Results and discussion

Comparison with experimental data

Perkins *et al.*[37] observed with their single DNA experiments in planar extensional flow that DNA deforms with different configurations: dumbell, kinked, half-dumbbell and folded and the extent of stretching was quite different for each configuration even for similar residence times in the stagnation point, *i.e.*, similar accumulated strain. De Gennes[15] called this behavior 'molecular individualism' and this can be attributed to the difference in initial configurations.[38] Certain initial configurations (*e.g.*, dumbbell configuration) are more adaptable to stretch even with small strain,[37,38] whereas other configurations such as a folded configuration take a longer time to be fully stretched. BD simulation[16] showed that a large strain is necessary to push ensemble stretching to steady state (strain $\sim$10; this strain results in $O(10^4)$ affine deformation). In real applications such as DLA, 'molecular individualism' can be an inherent hurdle to obtaining a uniformly stretched DNA distribution. The observation of 'molecular individualism' in non-homogeneous fields has been also recently observed.[12,13]

In Fig. 1(b) and (c) (also see ESI† to refer to the relative position of DNA in the channel), we show an example of 'molecular individualism' in the hyperbolic contraction at De = 7. We show two independent molecules whose center of mass are close to the centerline at the initial location. The molecule in Fig. 1(b) starts to move at the location where its center of mass is $(x_c/l_c, y_c/w_1) = (2.1,0.04)$, and the molecule in Fig. 1(c) is $(x_c/l_c, y_c/w_1) = (2.1, -0.09)$. The first snapshot in Fig. 1(b) and (c) approximately corresponds to the the moment when DNA starts to enter the funnel whereas the last snapshot corresponds to the moment when DNA head approaches the funnel exit (see ESI†). The difference between strains integrated along two field lines starting from (2.1,0.0) or $(2.1, \pm 0.2)$ up to the exit of hyperbolic region is $\sim$1% and the strain rate history *versus* x-coordinates is quite similar, *i.e.*, insensitive to initial y-location, in the region near the centerline as shown in Fig. 2(e). Thus, we expect that the kinematic histories experienced by the two molecules are quite similar. However, the molecules show quite different degree of stretching. This result shows that 'molecular individualism' is indeed relevant for the present problem.

As shown in Fig. 2, there are non-uniform entrance effects and thus, DNA molecules will experience different extent of strain according to their initial y-location as shown in Fig. 2(f). DNA molecules moving close to side-walls experience more strain than DNA molecules moving along centerlines. In the previous BD simulation in the planar extensional flows,[16] a strain of $\sim$10 is necessary to reach steady-state. If the net strain is larger than 10, it is expected that DNA stretching shows a uniform distribution. However, the strain in this work is limited to 4–7 (depending on the initial y-position), which is insufficient to reach steady-state stretching. DNA stretching is instead dependent upon the experienced strain which in turn depends upon its initial y-position. Therefore, DNA stretching is affected by the complexities of both 'molecular individualism' and non-uniform kinematic histories along its trajectory.

In Fig. 3, we compare the numerical prediction with experimental results for DNA stretching (x_{ex}), which shows good quantitative agreement for a wide range of De. There is a slight decrease in the experimental mean fractional stretching between De = 14 and 23 in contrast to simulation results and this may be attributed to limited statistics in the experiments.[10] Here, we measure the DNA stretching when the downstream-most part of a DNA passes the exit of the funnel ($x/l_c = -1$) to be consistent with the experimental analysis of ref. 10. As shown in Fig. 3(a), the results show that overall stretching is increased with increasing De. However, the extent of stretching does not significantly increase for De $>$ 23. As shown in Fig. 3(b) and (c), the probability distribution of fractional stretching is still broad even for De = 23, which can be attributed to 'molecular individualism' and non-uniform kinematic histories along different trajectories that reach modest net values of strain.

The good agreement of the present work with experimental data demonstrates that our BD-FEM has sufficient predictive capability to now design new channels. In the previous experimental work,[10] a gel-region in front of the contraction was introduced to generate 'preconditioned' DNA configurations more adaptable to stretching (partially stretched DNA) using a pseudo-tethering mechanism at the exit of the gel-region. Though the previous experimental approach showed a good performance in stretching DNA, it poses automation challenges. In the next two subsequent sections, we will explore two possibilities to enhance DNA stretching by changing channels: changing the shape of funnels and utilizing the effect of non-uniform kinematic history in the entrance region.

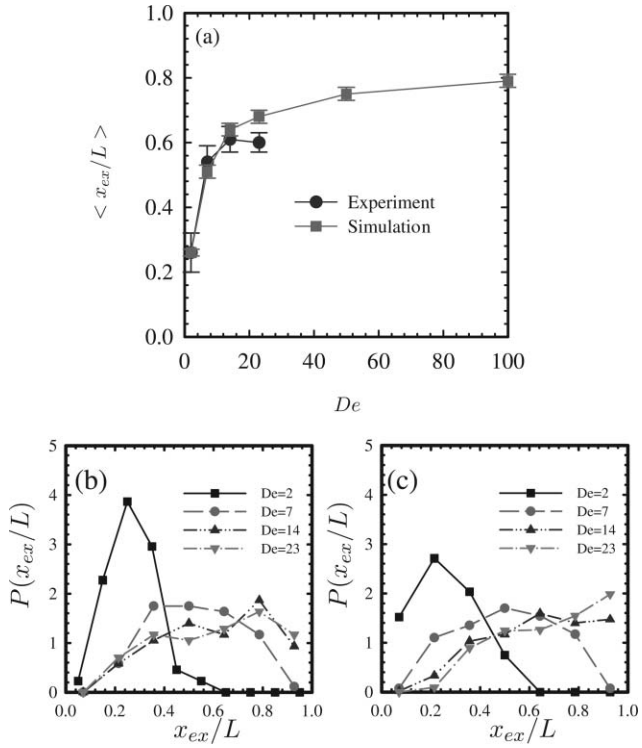

Fig. 3 (a) Comparison of mean fractional stretching ($< x_{ex}/L >$) obtained in experiments[10] and simulations. DNA stretching (x_{ex}) is measured when the downstream-most part of a DNA passes the exit of the funnel ($x/l_c = -1$). Probability distribution of mean fractional stretching: (b) experimental results and (c) simulation predictions.

Designing funnel shapes

In previous experimental work,[10] the hyperbolic funnel shape was used to generate a uniform strain rate. The ratio w_w/w_n used by Randall *et al.*[10] was (200/3.8 $\sim$ 52.6). We now survey the effect of strain rate histories on the DNA stretching using various funnel shapes, in which w_w and w_n are kept constant and equal to the values in the experimental study.[10]

Recently, the team from U.S. Genomics[11] experimentally investigated how different funnel shapes affect DNA stretching. In their work, DNA was hydrodynamically stretched using pressure-driven flows. The field kinematics are rather complicated in the pressure-driven contraction flow, which is a mixed flow composed of an elongational-dominant flow along the centerline and shear-dominant flow near the walls. Due to the shear flow, a tumbling motion of DNA can be generated near no-slip bondaries, which results in limited fractional stretching.[39] On the other hand, Larson showed that the shear flow can be used for the preconditioning of DNA.[17] The U.S. Genomics team speculated that upstream shearing of DNA was also important in their work.[11] Therefore, it is difficult to directly link kinematic analysis with DNA stretching in pressure-driven contraction flows. However, the field kinematics in electrophoresis involves only planar extensional fields and thus, is simpler to characterize with a kinematic analysis.

We present the detailed information for the four funnel shapes in Table 1 and adopt the same types of funnel shapes which were used by the U.S. Genomics team,[11] however, the absolute dimensions differ. We plot the strain rate along centerlines for four funnels in Fig. 4(a). Case I shows an abrupt increase at the exit of the funnel region, case II presents a rapidly developed strain rate in the entrance region, case III corresponds to the gradual ramping of strain rate up to the exit of the funnel region and case IV corresponds to an approximately constant strain rate, which is the hyperbolic geometry shown in Fig. 2. The strain histories *versus* x/l_c-coordinates for each funnel shape are presented in Fig. 4(b), where strain is integrated starting at $(x/l_c, y/w_1) = (2.1,0)$. DNA accumulates the same final strain along the centerline irrespective of funnel shape.

In Fig. 5(a)–(d), we present the mean fractional stretching *versus* the downstream-most coordinate of DNA ($-x_d/l_c$) for various De and funnel shapes, where $-x_d/l_c = 1$ corresponds to the exit of a funnel. Interestingly, in case I, significant DNA stretching only starts to occur near the exit of the funnel, whereas there is already significant DNA stretching from the

Table 1 Descriptions of the four funnels considered in this work. w_1 and w_2 are set to 100 μm and 1.9 μm, respectively. $w(x)$ denotes half of the funnel width. Case IV is consistent with the channel used by Randall *et al.*[10]

Cases	l_c/μm	Shapes of funnels	Schematics
Case I	80	$w(x) = (w_2 - w_1)/l_c \times (-x) + w_1$	
Case II	80	$w(x) = \dfrac{w_1}{\sqrt{(-x)/l_c\left((w_1/w_2)^2 - 1\right) + 1}}$	
Case III	80	$w(x) = \dfrac{w_1}{\left((-x)/l_c\left(\sqrt{w_1/w_2} - 1\right) + 1\right)^2}$	
Case IV	80	$w(x) = \dfrac{w_1}{((-x)/l_c(w_1/w_2 - 1) + 1)}$	

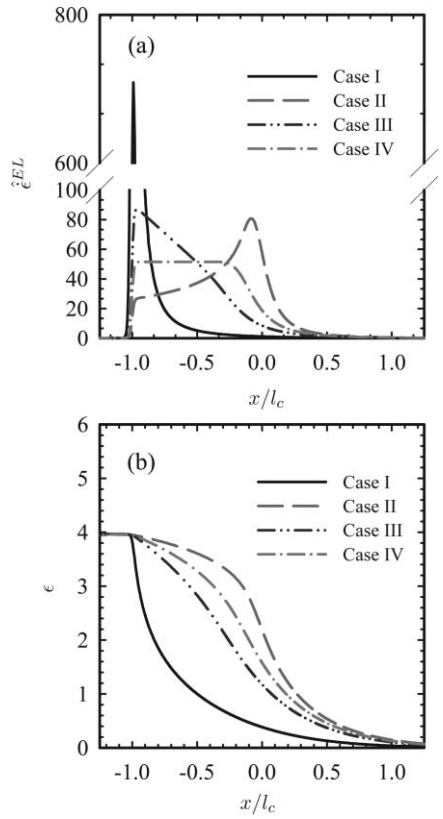

Fig. 4 Non-dimensionalized strain rate (a), and strain (b) for four funnel shapes along the channel centerline ($y = 0$). The detailed information for the funnels is provided in Table 1.

entrance region of the funnel in other cases (*e.g.*, the measured mean fractional stretching at $-x_d/l_c = 1$ is 0.25, 0.74, 0.61 and 0.68 at De = 23 for cases I, II, III, IV, respectively). We recall that De = 23 corresponds to the maximum De in the previous experiments.[10] However, as shown in Fig. 5(e), the maximum mean fractional stretching is similar irrespective of funnel shape. In Fig. 5(f), we also show the probability distribution of fractional stretching for four channel shapes at De = 23 and observe there is no appreciable difference among the four funnel shapes. However, the location where the maximum stretching occurs is quite different among the different funnel shapes (*e.g.*, the maximum stretching location is $-x_d/l_c = 1.70$, 1.19, 1.43 and 1.33 at De = 23 for cases I, II, III and IV, respectively).

For case I, as shown in Fig. 4(a), the strain rate is negligible almost up to the exit of the funnel and a high strain rate is abruptly developed near the funnel exit. Thus, DNA does not start to unravel until the exit of the funnel in case I. The overall mean fractional stretching continues to increase until $-x_c/l_c \approx 1.4 \sim 1.8$, which approximately corresponds to the location of downstream-most DNA segment ('head') when the upstream-most DNA segment ('tail') of a partially stretched DNA passes the exit of the funnel in case I. For example, the maximum mean fractional stretching is 0.76 at $-x_d/l_c \sim 1.7$ for De = 100 in case I and the location (1.7) is $\sim(0.76L + l_c)/l_c$. Physically this occurs because the DNA remains under tension when the 'head' is moving much faster than the 'tail', even though the strain rate is identically zero in the head region. The DNA will of course begin to relax once it is entirely in a region of constant $\mu\boldsymbol{E}$.

The previous argument can be bolstered by considering the various length scales in the problem. The DNA length scale (l_D) varies from an equilibrium radius of gyration (R_g) to a fully stretched contour length (L) depending upon its stretched state. In macroscopic devices where the device length scale (l_{dv}) is typically $\gg L$, DNA experiences a locally homogeneous strain rate at a molecular level and the local kinematics is a major factor in determining DNA deformation. The kinematics can be nonhomogeneous in a Lagrangian sense though. However, in microfluidic devices, the maximum DNA length scale (L) is sometimes comparable with l_{dv}; *e.g.* in the present geometries l_{dv} ($\sim$ the funnel length $l_c = 80$ μm) is comparable with the contour length $L = 71.4$ μm. This means that different sections of a stretched DNA molecule can simultaneously experience a spatially different strain rate. For example, a stretched DNA ($l_D \sim L$) spans a constant high $\mu\boldsymbol{E}$ region and low but nonhomogeneous region (the funnel) when the DNA head passes the funnel exit. However, DNA experiences a homogeneous field on a molecular level if $l_D \ll l_{dv}$, *e.g.* $l_D \sim R_g$ ($R_g/l_c \sim 0.02$ in this work) when the DNA initially begins to stretch. Thus in the present problem, the DNA can transition from deformation being initially governed by *local* kinematics to being governed by *non-local* kinematics. Recently, Underhill and Doyle[40] showed that the stretching of a DNA molecule can occur even when there is an abrupt step-change in the electrophoretic velocity—*i.e.* when a DNA passes from a region with constant $\mu\boldsymbol{E}$ to another with a larger, but constant, $\mu\boldsymbol{E}$. We shall refer to this as DNA stretching due to 'non-local field kinematics'. Though the present situation is rather different from the case that Underhill and Doyle[40] analyzed, in that the electrophoretic velocity varies rather smoothly in the funnel exit instead of a step-change, the difference of the electrophoretic velocity between DNA head and tail can result in the same effect as Underhill and Doyle[40] showed. Thus, DNA can continue to stretch due to the difference of electrophoretic velocity between the DNA head and tail when the DNA head enters a constant $\mu\boldsymbol{E}$ passing the funnel exit. This means that there can be extra stretching in addition to the DNA stretching due to the local strain rate in the funnel. We believe that most of the DNA stretching in case I is due to the 'non-local field kinematics'.

Case II is distinguishable from case I in that the stretching occurs mostly further upstream compared with case I. When $l_D \sim R_g$ (here $R_g/l_c \sim 0.02$), a molecule experiences a homogeneous strain rate on a molecular level and DNA initially deforms according to local field kinematics. Thus, high DNA stretching in case II (Fig. 5(b)) compared with other cases originates from the high strain rate in the entrance region. However, DNA experiences relatively low strain rate as the DNA head moves towards the funnel exit and the slopes of curves in Fig. 5(b) become blunt near $-x_d/l_c \sim 1$. As the DNA head passes the funnel exit, DNA stretching due to non-local field kinematics starts to occur, which results in continued stretching downstream ($-x_d/l_c > 1.0$). However, in this case, DNA stretching due to non-local field kinematics is not large.

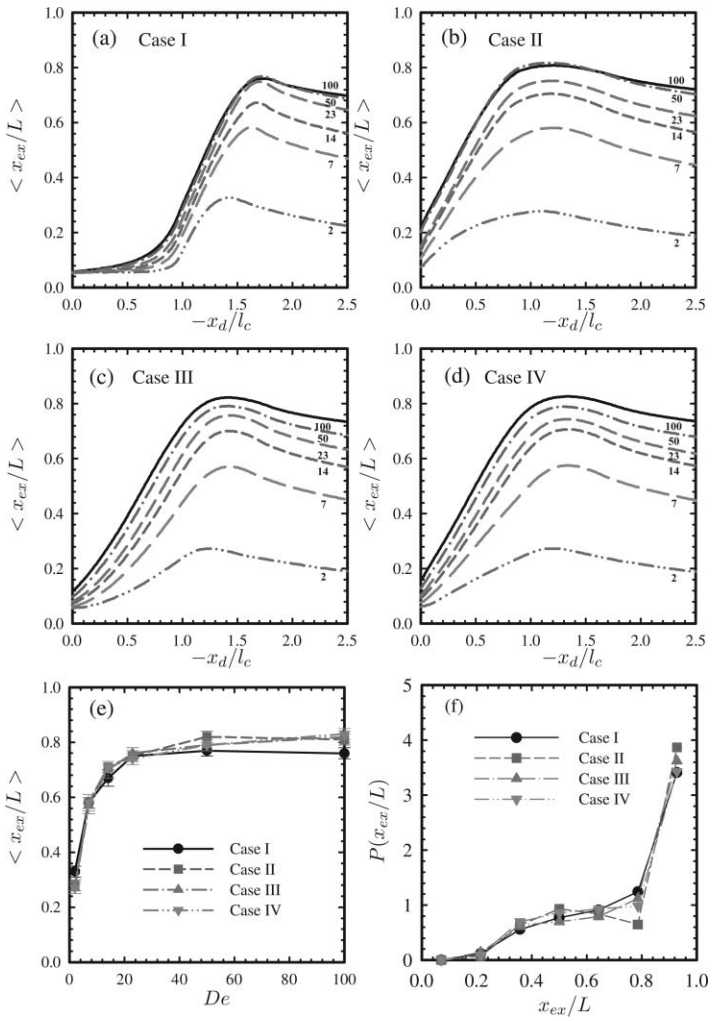

Fig. 5 (a)–(d) The predicted mean fractional stretching ($< x_{ex}/L >$) *versus* $-x_d/l_c$ for four funnels shown in Table 1. $-x_d/l_c = 0$ is the starting point of the hyperbolic region and $-x_d/l_c = 1$ corresponds to the exit of the funnel. (a): Case I, (b): case II, (c): case III and (d): case IV. The label attached to each curve shows the corresponding De. (e) The maximum mean fractional stretching ($< x_{ex}/L >$) *versus* De. (f) Comparison of probability distribution at maximum mean fractional stretching at De = 23.

This can be attributed to the fact that the DNA is already appreciably stretched when it exits the funnel and DNA stretching due to non-local kinematics only plays a role in preserving the stretched state, which is manifested in the flat peaks in Fig. 5(b).

Cases III and IV can be considered to be intermediate steps between cases I and II. The stretching in cases III and IV is smaller than case II in the funnel entrance (*cf.* Fig. 5, the increasing order of stretching in this region is I, III, IV and II), since the local strain rate and accumulated strain is smaller than case II. The order of stretching extent in the entrance region is consistent with the order of local strain rate and strain in the entrance region (*cf.* Fig. 4(a)). Similar to cases I and II, the stretching in cases III and IV continues to occur past the funnel exit due to non-local kinematics. However, the maximum mean fractional stretching is similar irrespective of funnel shape and the values become saturated with increasing De as shown in Fig. 5(e).

For non-local kinematics involving a rapid change in velocity, Underhill and Doyle[40] proposed two limits according to the residence time scale (t_r) over which the DNA moves from a region with low electrophoretic velocity μE_l to a high electrophoretic velocity μE_h. In brief, there are two limits: (1) when t_r is small, DNA stretching is only a function of $(\mu E_h - \mu E_l)/\mu E_l$ and (2) when t_r is large, DNA stretching becomes similar to a pseudo-tethered DNA and stretching is proportional to $(\mu E_h - \mu E_l)/l_D \times \tau$. In order to increase De, μE_h must increase. However, our geometry imposes a constraint that $\mu E_h/\mu E_l \sim w_w/w_n$. Therefore, as De increases, the convective velocity increases, which naturally leads to a smaller t_r (scenario (1)). For small t_r (high De), the stretching due to non-local kinematics is limited to a value dependent upon $\sim (\mu E_h - \mu E_l)/\mu E_l \sim (w_w/w_n - 1)$, which is constant irrespective of funnel shape. This is most probably the reason why the maximum stretching in funnels becomes saturated with increasing De instead of gradual increasing in Fig. 5(e). This saturation occurs above De of $\sim$23. Below De of $\sim$23, the t_r is not small enough to be in (1), therefore the maximum mean stretching is a function of De.

The team from U.S. Genomics[11] also considered the same four funnel shapes as the present work to investigate the effect of different funnel shapes. The DNA size (185 kbp) used in their work was also similar to the DNA size (169 kbp) of the present work. They observed that the probability distribution of stretching was quite different among funnel shapes.[11] In their experiments, the case III-type funnel showed the best performance in that the probability distribution of stretching was skewed towards high vales. However, in our work, there is no appreciable difference in the stretch probability distribution at high De (*cf.* Fig. 5(f)). This difference can be mainly attributed to the difference in field kinematics since the pressure-driven flow is a mixed flow composed of elongational and shear flows, and the role of shear flow near the solid walls can differ in determining stretching depending on the funnel shapes in pressure-driven flow used by the team from U.S Genomics.[11] This demands further study to clarify how a mixed flow affects DNA stretching in different flow geometries. It is also not clear that the location at which the stretching was measured by the team from U.S. Genomics[11] corresponds to the location with the maximum mean fractional stretching (the location used in the present work) since they measured the stretching one-contour length downstream from the funnel exit.

Up to now we have investigated how strain rate history affects DNA stretching. The maximum mean fractional stretching is not greatly affected by funnel shape. However, the curves of mean fractional stretching *versus* $-x_d/l_c$ are quite different among funnel shapes. We observe that there is a rather broad flat region with highly stretched DNA for case II. This will be useful information for practical implementation of DLA, *e.g.*, in the placement of the detectors of fluorescent probes. In the next section, we explore another choice for the channel design which is inspired by the kinematic analysis presented in Fig. 2(f).

Side feeding

In Fig. 2, we observed the non-uniform distribution of strain rate in the entrance region. Here, we will more thoroughly investigate the effect of this non-uniformity on the DNA stretching and we explore another design choice to exploit the non-uniformity in the entrance region. We chose two funnels shapes (case II and IV in Table 1) since case II showed a rather broad interval with highly stretched state and case IV was

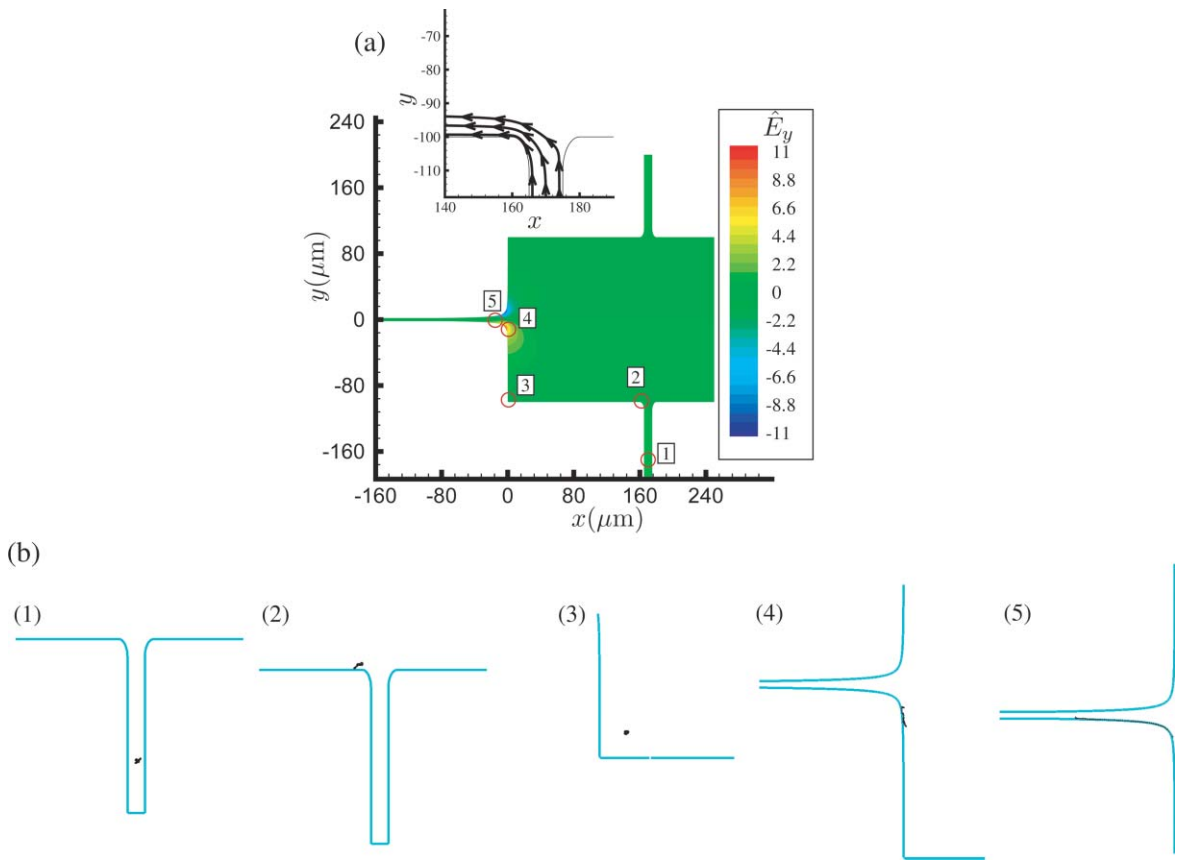

Fig. 6 (a) A hyperbolic geometry with side-feeding. Contours correspond to the *y*-component of the dimensionless electric field. For symmetry, a geometry with two branches (lower and upper) is considered, and it is set up that the center of mass of DNA starts to move at $y/l_c = -2.1$ in the lower branch. Circles with a number correspond to the sampling region for DNA configuration snapshots. The inset is the magnified view around the region (2) and the lines with arrows in the inset are field lines around the lower branch. (b) DNA configurations at De = 14 when DNA passes the regions, (1), (2), (3), (4), (5) and (6) as shown in (a). Times between two successive snapshots, (1)–(2), (2)–(3), (3)–(4) and (4)–(5) are 4.60, 9.21, 4.41 and 0.12 , respectively.

originally considered in the previous experimental work.[10] We present strain rate and strain distribution along three field lines for case II (see ESI†) and case IV (Fig. 2(e), (f)), where the three field lines commonly start at $(x/l_c,y/w_1)$ = (2.1,0.0), (2.1,0.5) and (2.1,0.95). Fig. 2(e) and (f) are obtained along the three field lines shown in Fig. 2(d). As shown in Fig. 2(f) (also see ESI† for case II), there is extra strain increase near the entrance of the contraction (x = 0) for field lines close to the side-walls. This increase partially originates from the increased strain rate at the side-walls in the entrance region and is also due to a rather large residence time along curved field lines near side-walls as shown Fig. 2(d). As shown in Fig. 2(f) (also see ESI† for case II), we observe that the strain along the centerline is $\ln(w_1/w_2) \sim 4$, and the difference of strains between the centerline and side-wall trajectories amounts to 3, which is quite a large difference (strain $\sim$ 3 results in $\sim$20-fold larger affine deformation). Thus, we employ a new design which takes advantage of the increased strain along fields lines passing near side-walls. This can be realized with the introduction of a side-feeding port. We designed two side branches corresponding to $(x/l_c,y/w_1) = (2.1, \pm 1.0)$ with the width of 10 μm in case II, IV. The length of the branch is set to w_1. We present an example in Fig. 6(a), which corresponds to case II with a branch. We assume that the same potential is imposed on both side branches and the wide inlet, and the ground condition is imposed on the outlet. DNA is initially randomly distribution along the line from $(x/l_c,y/w_1)$ = (2.06,−1.7) to $(x/l_c,y/w_1)$ = (2.19,−1.7) and DNA penetrating through walls is rejected.

In Fig. 6(a), the contour shows the normalized y-component of electric field, which shows that there is a rather strong electric field towards the inner contraction near the entrance region. In the inset of Fig. 6(a), we present the field lines around the region (2). The field lines from the branch pass near the side-wall boundary and thus, it is expected that DNA from the branch move near the side wall. As shown in Fig. 6(b), DNA molecules move along side-walls and experience higher stretching along the curved field line in the entrance region. We computed the maximum mean ensemble-averaged stretching for cases II and IV with branches and compared those results with the cases without a branch. As shown in Fig. 7(a), there is a dramatic increase in DNA stretching for the side-feeding cases. For comparison, we added data for steady-state ensemble-averaged stretch in a homogeneous planar elongational field. One would anticipate that these data correspond to the maximum mean fractional extension attainable for

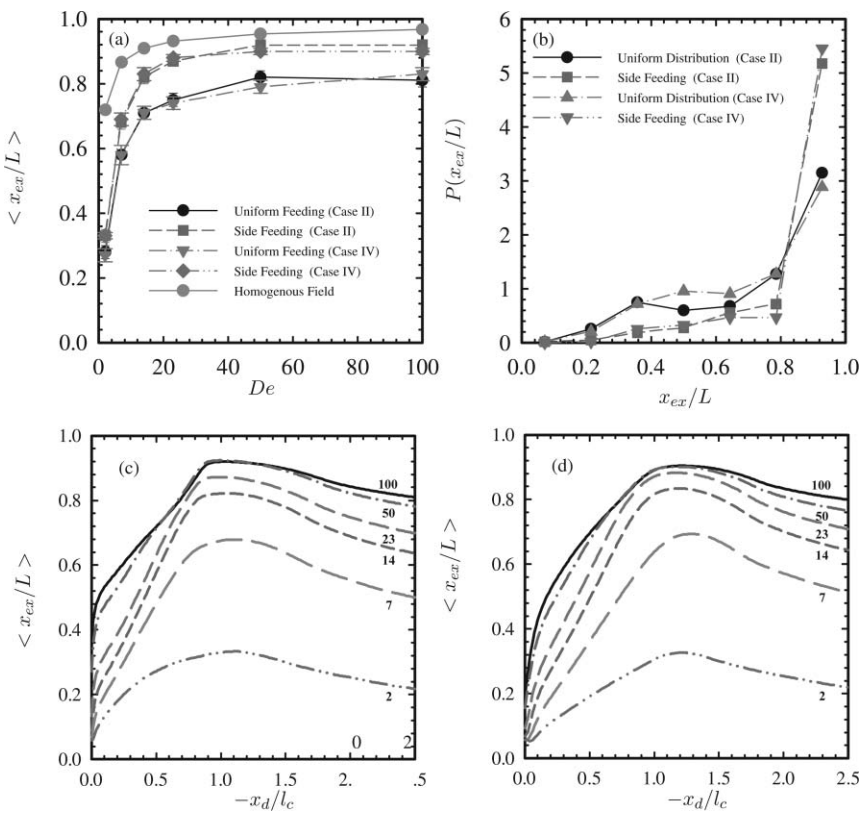

Fig. 7 (a) Comparison of the predicted maximum mean fractional stretching between cases II and IV with side-feeding and uniform distribution cases. The data for uniform distribution is from Fig. 5(e). The data for 'homogeneous field' stand for the ensemble-averaged DNA stretching at steady state in a homogenous planar extensional field. (b) Comparison of probability distribution of the maximum mean fractional stretching between uniform distribution and side feeding at De = 14. The predicted mean fractional stretching ($< x_{ex}/L >$) *versus* $-x_d/l_c$ for cases with side-feeding. (c): case II with side-feeding and (d): case IV with side-feeding. The label attached to each curve shows the corresponding De. $-x_d/l_c = 0$ is the starting point of the hyperbolic region and $-x_d/l_c = 1$ corresponds to the exit of the funnel.

given De. We observe that the mean fractional stretching with side-feeding geometries becomes quite comparable with the steady-state (infinite strain) cases at high De. For example, as shown Fig. 7(b) (De = 14), the probability distribution of fractional stretching also becomes narrower compared with the original channels without a branch, where the probability distribution for the steady-state in a homogeneous field is omitted since the whole ensemble exits in the interval between 0.8 and 1.0 (*i.e.* there would be a single peak in Fig. 7(b)). We attribute the enhancement of DNA stretching to the higher strain experienced along the field lines near side-walls. Of course non-local kinematics could potentially play a role. However, most stretching occurs before the funnel exit ($-x_d/l_c = 1$) for theses cases with side-feeding as shown in Fig. 7(c) and (d). Thus, we can conclude that the stretching due to non-local kinematics is negligible to enhance the mean fractional stretching for theses cases.

The present study shows that the strategy to design a device for optimal DNA stretching can be conjectured from a kinematic analysis. BD-FEM simulations show that an enhancement of DNA stretching is possible with a simple change of channel design including side-feeding. The present scheme can be also combined with a gel to possibly enhance DNA stretching.

Conclusion

A detailed kinematic analysis is presented for the hyperbolic DNA stretching geometry including the distribution of local strain rate, and principal axes of stretching and compression. We show that there are non-uniform fields in the entrance region, which result in a non-uniform strain distribution along different field lines. We directly compared the numerical BD-FEM simulation to experimental data in a hyperbolic geometry and found good agreement on both qualitative and quantitative levels. The broad distribution of the probability distribution of the fractional stretching can be attributed to 'molecular individualism' and also the vastly different kinematic histories along different trajectories.

We investigated the impact of different kinematic histories on the DNA stretching with four funnel shapes. The maximum mean fractional stretching is similar irrespective of funnel shape. Finally, we surveyed the effect of non-uniform kinematic histories along the initial center of mass y-locations. We found that there is increased strain for field lines near the side-walls. Based on this observation and the study about the funnel shape, we proposed a new channel design such that the channel has side branches. We predicted that there is a dramatic increase in DNA stretching in the side-feeding geometry.

We expect that the proposed new design will be used for a practical DNA stretching device with enhanced performance and the present methodology will be useful for further optimization.

Acknowledgements

The authors are gratefully thankful to Dr Greg C. Randall for useful discussions about the experimental system and also to Dr Patrick T. Underhill for helpful discussions including DNA stretching problem in step-change of electrophoretic velocity. This work was supported by U.S. Genomics and also NSF CAREER Award No. CTS-0239012.

References

1 J.-L. Viovy, *Rev. Mod. Phys.*, 2000, **72**, 813.
2 E. Y. Chan, N. M. Goncalves, R. A. Haeusler, A. J. Hatch, J. W. Larson, A. M. Maletta, G. R. Yantz, E. D. Carstea, M. Fuchs, G. G. Wong, S. R. Gullans and R. Gilmanshin, *Genome Res.*, 2004, **14**, 1137.
3 K. M. Phillips, J. W. Larson, G. R. Yantz, C. M. D'Antoni, M. V. Gallo, K. A. Gillis, N. M. Goncalves, L. A. Neely, S. R. Gullans and R. Gilmanshin, *Nucleic Acids Res.*, 2005, **33**, 5829.
4 J. Lin, R. Qi, C. Aston, J. Jing, T. S. Anantharaman, B. Mishra, O. White, M. J. Daly, K. W. Minton, J. C. Venter and D. C. Schwartz, *Science*, 2003, **301**, 1515.
5 D. C. Schwartz, X. Li, L. I. Hernandez, S. P. Ramnarain, E. J. Huff and Y.-K. Wang, *Science*, 1993, **262**, 110.
6 E. T. Dimalanta, A. Lim, R. Runnheim, C. Lamers, C. Churas, D. F. Forrest, J. J. de Pablo, M. D. Graham, S. N. Coppersmith, S. Goldstein and D. C. Schwartz, *Anal. Chem.*, 2004, **76**, 5293.
7 J. O. Tegenfeldt, C. Prinz, H. Cao, S. Chou, W. W. Reisner, R. Riehn, Y. M. Wang, E. C. Cox, J. C. Sturm, P. Silberzan and R. H. Austin, *Proc. Natl. Acad. Sci. U. S. A.*, 2004, **101**, 10979.
8 R. Riehn, M. Lu, Y.-M. Wang, S. F. Lim, E. C. Cox and R. H. Austin, *Proc. Natl. Acad. Sci. U. S. A.*, 2005, **102**, 10012.
9 J. O. Tegenfeldt, O. Bakajin, C. -F. Chou, S. S. Chan, R. Austin, W. Fann, L. Liou, E. Chan, T. Duke and E. C. Cox, *Phys. Rev. Lett.*, 2001, **86**, 1378.
10 G. C. Randall, M. Schultz Kelly and P. S. Doyle, *Lab Chip*, 2006, **6**, 516.
11 J. W. Larson, G. R. Yantz, R. Charnas, C. M. D'Antoni, M. V. Gallo, K. A. Gillis, L. A. Neely, K. M. Phillips, G. G. Wong, S. R. Gullans and R. Gilmanshin, *Lab Chip*, 2006, **6**, 1187.
12 G. C. Randall and P. S. Doyle, *Macromolecules*, 2005, **38**, 2410.
13 J. M. Kim and P. S. Doyle, *J. Chem. Phys.*, 2006, **125**, 074906.
14 G. C. Randall and P. S. Doyle, *Phys. Rev. Lett.*, 2004, **93**, 1137.
15 P. G. De Gennes, *Science*, 1997, **276**, 1999.
16 P. S. Doyle, E. S. Shaqfeh and A. P. Gast, *J. Fluid Mech.*, 1997, **334**, 251.
17 R. G. Larson, *J. Non-Newtonian Fluid Mech.*, 2000, **94**, 37.
18 C. Bustamante, J. F. Marko, E. D. Siggia and S. Smith, *Science*, 1994, **265**, 1599.
19 D. Long, A. V Dobrynin, M. Rubinstein and A. Ajdari, *J. Chem. Phys.*, 1998, **108**, 1234.
20 R. H. Zimm, *J. Chem. Phys.*, 1956, **24**, 269.
21 S. Ferree and W. B. Harvey, *Biophys. J.*, 2004, **85**, 2539.
22 N. Liron and S. Mochon, *J. Eng. Math.*, 1976, **10**, 287.
23 T. Tlusty, *Macromolecules*, 2006, **39**, 3927.
24 A. Balducci, P. Mao, J. Han and P. S. Doyle, *Macromolecules*, 2006, **39**, 6237.
25 O. B. Bakajin, T. A. J. Duke, C. F. Chou, S. S. Chan, R. H. Austin and E. C. Cox, *Phys. Rev. Lett.*, 1998, **80**, 2737.
26 Y.-L. Chen, M. D. Graham, J. J. de Pablo, G. C. Randall, M. Gupta and P. S. Doyle, *Phys. Rev. E: Stat. Phys., Plasmas, Fluids, Relat. Interdiscip. Top.*, 2004, **70**, 060901.
27 P. G. De Gennes, *J. Chem. Phys.*, 1974, **60**, 5030.
28 E. S. G. Shaqfeh, *J. Non-Newtonian Fluid Mech.*, 2005, **130**, 1.
29 A. J. Szeri, S. Wiggins and L. G. J. Leal, *J. Fluid Mech.*, 1991, **228**, 207.
30 N. Minc, C. Fütterer, K. D. Dorfman, A. Bancaud, C. Gosse, C. Goubault and J.-L. Viovy, *Anal. Chem.*, 2004, **76**, 15.
31 P. T. Underhill and P. S. Doyle, *J. Non-Newtonian Fluid Mech.*, 2004, **122**, 3.
32 J. F. Marko and E. D. Siggia, *Macromolecules*, 1995, **28**, 8759.

33 R. M. Jendrejack, M. D. Graham and J. J. de Pablo, *J. Chem. Phys.*, 2002, **116**, 7752.
34 R. M. Jendrejack, D. C. Schwartz, M. D. Graham and J. J. de Pablo, *J. Chem. Phys.*, 2003, **119**, 1165.
35 R. M. Jendrejack, D. C. Schwartz, J. J. de Pablo and M. D. Graham, *J. Chem. Phys.*, 2004, **120**, 2513.
36 D. Heyes and J. Melrose, *J. Non-Newtonian Fluid Mech.*, 1993, **46**, 1.
37 T. T. Perkins, D. E. Smith and S. Chu, *Science*, 1997, **276**, 2016.
38 D. E. Smith and S. Chu, *Science*, 1998, **281**, 1335.
39 D. E. Smith, H. P. Bobcock and S. Chu, *Science*, 1999, **283**, 1724.
40 P. T. Underhill and P. S. Doyle, manuscript in preparation.